Wind-driven lateral circulation in a stratified estuary and its effects on the along-channel flow

Yun Li[1] and Ming Li[1]

Received 13 December 2011; revised 2 July 2012; accepted 17 July 2012; published 5 September 2012.

[1] In the stratified rotating estuary of Chesapeake Bay, the Ekman transport drives a counterclockwise lateral circulation under down-estuary winds and a clockwise lateral circulation under up-estuary winds (looking into estuary). The clockwise circulation is about twice as strong as the counterclockwise circulation. Analysis of the streamwise vorticity equation reveals a balance among three terms: titling of the planetary vorticity by vertical shear in the along-channel current, baroclinic forcing due to sloping isopycnals at cross-channel sections, and turbulent diffusion. The baroclinic forcing is highly asymmetric between the down- and up-estuary winds. While the counter-clockwise lateral circulation tilts isopycnals vertically and creates lateral barolinic pressure gradient to oppose the Ekman transport under the down-estuary wind, the clockwise circulation initially flattens the isopycnals and the baroclinic forcing reinforces the Ekman transport under the up-estuary wind. The Coriolis acceleration associated with the lateral flows is of the first-order importance in the along-channel momentum balance. It has a sign opposite to the stress divergence in the surface layer and the pressure gradient in the bottom layer, thereby reducing the shear in the along-channel current. Compared with the non-rotating system, the shear reduction is about 30–40%. Two summary diagrams are constructed to show how the averaged streamwise vorticity and along-channel current shear vary with the Wedderburn (W) and Kelvin (Ke) numbers.

Citation: Li, Y., and M. Li (2012), Wind-driven lateral circulation in a stratified estuary and its effects on the along-channel flow, *J. Geophys. Res.*, *117*, C09005, doi:10.1029/2011JC007829.

1. Introduction

[2] The wind-driven circulation in an estuary has previously been interpreted in terms of the competition between the wind stress and barotropic pressure gradient due to sea level setup in the along channel direction [*Weisberg and Sturges*, 1976; *Wang*, 1979; *Garvine*, 1985; *Janzen and Wong*, 2002]. In a rectangular estuary or a stratified estuary where the buoyancy flux is strong, the along-channel flow consists of a vertically sheared two-layer circulation: downwind currents in the surface layer and upwind currents in the bottom layer [e.g., *Chen and Sanford*, 2009; *Reyes-Hernández and Valle-Levinson*, 2010]. In estuaries with lateral variations of bathymetry, the depth-dependence in the longitudinal momentum balance leads to laterally sheared three-layer circulation: downwind currents on the shallow shoals and upwind flows in the center deep channel [e.g., *Wong*, 1994; *Friedrichs and Hamrick*, 1996]. However, this picture of wind-driven circulation in a stratified rotating estuary is incomplete.

[3] Several studies have shown that along-channel winds can drive strong lateral Ekman flows and isopycnal movements, generating upwelling/downwelling at shallow shoals [*Malone et al.*, 1986; *Sanford et al.*, 1990; *Wilson et al.*, 2008; *Scully*, 2010]. These lateral motions are fundamental to estuarine dynamics because they transport momentum [*Lerczak and Geyer*, 2004; *Scully et al.*, 2009], alter stratification [*Lacy et al.*, 2003; *Li and Li*, 2011] and transport sediment [*Geyer et al.*, 2001; *Chen et al.*, 2009]. For example, *Li and Li* [2011] showed that the wind-driven lateral circulation causes lateral straining of the density field which offsets the effects of longitudinal straining. Furthermore, the lateral circulations provide an exchange pathway for biologically important materials such as nutrients and oxygen, especially through lateral upwelling and downwelling [*Malone et al.*, 1986; *Sanford et al.*, 1990; *Reynolds-Fleming and Luettich*, 2004]. A recent study suggests that, in Chesapeake Bay, the wind-driven lateral exchange of oxygen between shoal regions and deeper hypoxic areas is more important than direct turbulent mixing through the pycnocline [*Scully*, 2010]. Despite these interesting studies, the dynamics of wind-driven lateral circulations in stratified estuaries of varying width are still poorly understood. A simple scaling

[1]Horn Point Laboratory, University of Maryland Center for Environmental Science, Cambridge, Maryland, USA.

Corresponding author: Y. Li, Horn Point Laboratory, University of Maryland Center for Environmental Science, 2020 Horn Point Rd., Cambridge, MD 21613, USA. (yunli@umces.edu)

suggests that the redistribution of momentum by lateral flows is expected to play a larger role in narrow estuaries where lateral gradients in the along-channel momentum are bigger. However, wider estuaries are expected to have a stronger lateral response to the along-channel wind-forcing because of rotation.

[4] There have been a series of interesting studies on the dynamics of lateral circulations in tidally driven estuaries. Several mechanisms have been proposed, including differential advection [*Nunes and Simpson*, 1985; *Lerczak and Geyer*, 2004], bottom Ekman layer [*Scully et al.*, 2009], diffusive boundary layer on a slope [*Chen et al.*, 2009], channel curvature [*Chant*, 2002] and lateral salinity gradient resulting from the presence of stratification [*Lerczak and Geyer*, 2004; *Scully et al.*, 2009; *Cheng et al.*, 2009]. Using a numerical model of an idealized estuarine channel, *Lerczak and Geyer* [2004] demonstrated that the lateral flows are driven primarily by differential advection and cross-channel density gradients, and exhibit strong flood-ebb and spring-neap variability. In a subsequent study of Hudson River estuary, *Scully et al.* [2009] showed that nonlinear tidal advection by lateral Ekman transport generates one-cell lateral circulation over flood-ebb tidal cycle, as found in an analytic model of *Huijts et al.* [2009]. Most of these previous studies focused on the analysis of the along-channel and cross-channel momentum balance. Since the leading-order momentum balance in the cross-channel direction is the thermal-wind balance, *Scully et al.* [2009] discussed the ageostrophic term and provided insightful discussions on the interactions between the lateral Ekman flows and lateral baroclinic pressure gradient. In this paper we develop a new approach to investigate the dynamics of lateral circulations. We will investigate the streamwise (along-channel) vorticity which provides a scalar representation of the lateral circulation, and conduct diagnostic analysis of the streamwise vorticity equation to identify the generation and dissipation mechanisms.

[5] A major motivation for studying the lateral circulation in estuaries is the need to understand its effects on the along-channel estuarine exchange flows. In tidally driven estuaries, recent modeling investigations have demonstrated that the lateral advection is of the first-order importance in the along-channel momentum balance [*Lerczak and Geyer*, 2004; *Scully et al.*, 2009; *Cheng et al.*, 2009]. *Burchard et al.* [2011] and *Burchard and Schuttelaars* [2012] decomposed the estuarine residual circulation into contributions from processes such as tidal straining circulation, gravitational circulation, advectively driven circulation, and horizontal mixing circulation. They found that the lateral advection can be a major driving force for the estuarine circulation in some estuaries. This motives us to examine the effects of the lateral flows on the wind-driven flows in the along-channel direction. It will be shown that the Coriolis acceleration associated with the lateral circulation is of the first-order importance in the along-channel momentum balance. Unlike the nonlinear advection term which augments the along-channel flows, however, the Coriolis acceleration reduces the shear in the along-channel current.

[6] Using Chesapeake Bay as an example of a partially mixed/stratified estuary, *Li and Li* [2011] investigated how the wind-driven lateral circulation causes the lateral straining of density field and how this lateral straining offsets the effects of longitudinal straining to reduce the stratification-reduction asymmetry between the down- and up-estuary winds. This is a companion paper where we examine the vorticity dynamics of the wind-driven lateral circulation and its effects on the along-channel flows. The plan for this paper is as follows. In Section 2 we describe the model configuration and introduce the analysis approach. Section 3 is devoted to the analysis of the streamwise vorticity equation while Section 4 is devoted to the analysis of the along-channel momentum balance. In Section 5, we summarize the model results in a non-dimensional parameter space consisting of the Wedderburn (W) and Kelvin (Ke) numbers.

2. Model Configuration and Analysis Approach

[7] To study wind-driven lateral flows, we use a 3D hydrodynamic model of Chesapeake Bay based on ROMS (Regional Ocean Modeling System) [*Li et al.*, 2005, 2007; *Zhong and Li*, 2006; *Zhong et al.*, 2008; *Li and Zhong*, 2009]. The model domain covers 8 major tributaries and a part of the coastal ocean to allow free exchange across the bay mouth (Figure 1). The total number of grid points is 120×80. The model has 20 layers in the vertical direction. A quadratic stress is exerted at the bed, assuming that the bottom boundary layer is logarithmic over a roughness height of 0.5 mm. The vertical eddy viscosity and diffusivity are computed using the *k-kl* turbulence closure scheme [*Warner et al.*, 2005] with the background diffusivity and viscosity set at 10^{-5} m^2 s^{-1}. The horizontal eddy viscosity and diffusivity are set to 1 m^2 s^{-1}. The model is forced by tides at the offshore boundary, by freshwater inflows at river heads, and by winds across the water surface. The open-ocean boundary condition consists of Chapman's condition for surface elevation, Flather's condition for barotropic velocity, Orlanski-type radiation condition for baroclinic velocity, and a combination of radiation condition and nudging (with a relaxation time scale of 1 day) for scalars [*Marchesiello et al.*, 2001].

[8] In this paper we conduct process-oriented idealized modeling studies. At the open-ocean boundary, the model is forced by M_2 tides only and salinity is fixed at 30 psu. The total river discharge into the Bay is kept at the long-term average of 1500 m^3 s^{-1} and is distributed to eight major tributaries according to observations: Susquehanna (51%), Patapsco (3.67%), Patuxent (3.67%), Potomac (18%), Rappahannock (4%), York (2%), James (14%), and Choptank (3.67%) [cf., *Guo and Valle-Levinson*, 2008]. We first run the model without wind-forcing for 5 years so that the circulation and stratification in the Bay reaches a steady state. We then force the model with the along-channel (southward or northward) winds of varying amplitudes and directions. Cross-channel (eastward or westward) winds are not considered here because of fetch limitation. The wind stress is spatially uniform and is given by

$$\tau_W = \begin{cases} \tau_p \sin[\omega(t-25)] & 25 \le t \le 27.5 \\ 0 & \textit{other times} \end{cases}, \tag{1}$$

where τ_w is the along-channel wind stress, t the time (days), $\omega = \dfrac{2\pi}{5\ \text{day}}$ the frequency of the wind-forcing, and τ_p the peak wind stress. Positive τ_W corresponds to up-estuary

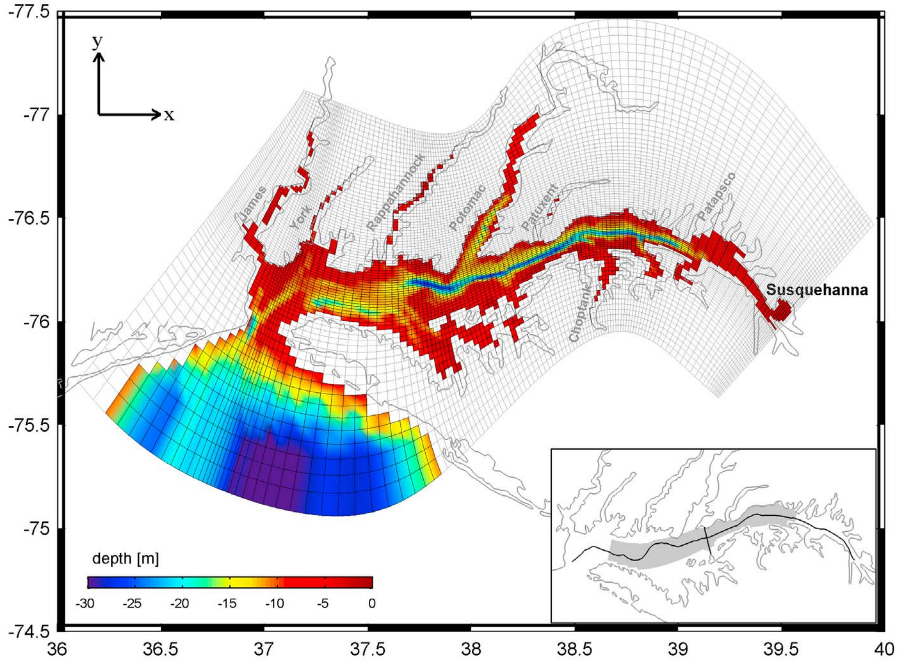

Figure 1. Bathymetry of Chesapeake Bay and its adjacent coastal shelf. Major tributaries are marked. Depths are in meters. The shaded areas in the insert are used for calculating volume-averaged quantities in this study. The solid lines represent the along-channel and cross-channel transects.

(northward) winds whereas negative τ_W corresponds to down-estuary (southward) winds. The maximum wind stress magnitude τ_p ranges from 0.005 to 0.25 Pa, with the corresponding range of 2.35 to 12.27 m s^{-1} for the wind speed (Table 1).

[9] Previous investigations of lateral circulations in estuaries have mainly focused on the analysis of the cross-channel momentum equation [e.g., *Lerczak and Geyer*, 2004; *Scully et al.*, 2009]

$$\underbrace{\frac{\partial v}{\partial t}}_{\text{acceleration}} = \underbrace{-fu}_{\substack{\text{Coriolis}\\\text{acceleration}}} \underbrace{-\frac{1}{\rho}\frac{\partial P}{\partial y}}_{\text{pressure gradient}} \underbrace{-\left(u\frac{\partial v}{\partial x}+v\frac{\partial v}{\partial y}+w\frac{\partial v}{\partial z}\right)}_{\text{nonlinear advection}} + \underbrace{\frac{\partial}{\partial z}\left(K_V\frac{\partial v}{\partial z}\right)}_{\text{stress divergence}}, \tag{2}$$

where (u, v, w) are the velocity components in the along-channel (x-), cross-channel (y-) and vertical (z-) directions. Consistent with the previous definition of the Wedderburn number [*Chen and Sanford*, 2009; *Li and Li*, 2011], the positive x axis is pointed northward, the positive y axis is pointed westward, and the positive z axis is pointed upward. The lateral pressure gradient consists of two terms: lateral sea level slope and lateral density gradient.

[10] Here we adopt a new approach by analyzing the equation of the streamwise (along-channel) vorticity defined as $\omega_x = \frac{\partial w}{\partial y} - \frac{\partial v}{\partial z}$. If one looks into estuary in the northern hemisphere, a clockwise/counterclockwise lateral circulation corresponds to positive/negative ω_x. The strength of lateral circulation is represented by the absolute value of ω_x. The equation for ω_x is given by

$$\begin{aligned}\frac{d\omega_x}{dt} = {} & f\frac{\partial u}{\partial z} + \left(\omega_x\frac{\partial u}{\partial x}+\omega_y\frac{\partial u}{\partial y}+\omega_z\frac{\partial u}{\partial z}\right) \\ & + \left[\frac{\partial}{\partial y}\left(-\frac{1}{\rho}\frac{\partial P}{\partial z}\right) - \frac{\partial}{\partial z}\left(-\frac{1}{\rho}\frac{\partial P}{\partial y}\right)\right] \\ & + \frac{\partial}{\partial x}\left[\frac{\partial}{\partial y}\left(K_H\frac{\partial w}{\partial x}\right) - \frac{\partial}{\partial z}\left(K_H\frac{\partial v}{\partial x}\right)\right] \\ & + \frac{\partial}{\partial y}\left[\frac{\partial}{\partial y}\left(K_H\frac{\partial w}{\partial y}\right) - \frac{\partial}{\partial z}\left(K_H\frac{\partial v}{\partial y}\right)\right] \\ & + \frac{\partial}{\partial z}\left[\frac{\partial}{\partial y}\left(K_V\frac{\partial w}{\partial z}\right) - \frac{\partial}{\partial z}\left(K_V\frac{\partial v}{\partial z}\right)\right],\end{aligned} \tag{3}$$

where (ω_y, ω_z) are the vorticity components in the cross-channel and vertical directions, ρ the density, P the pressure, and K_H and K_V are eddy viscosity in the vertical and horizontal directions [cf., *Kundu and Cohen*, 2004]. Equation (3) shows that the streamwise vorticity ω_x can be generated by tilting of the planetary vorticity f due to the vertical shear in the along-channel current, by vortex stretching/tilting, by baroclinicity in the cross-channel section (misalignment of pressure and density surfaces), and is diffused by subgrid-scale turbulent flows.

[11] Making the Boussinesq approximation for the horizontal momentum equations and the hydrostatic assumption for the vertical momentum equation, and assuming that the

Table 1. Idealized Wind Experiments[a]

Wind Stress (Pa)	Wind Speed (m/s)	Ke = 0.00		Ke = 1.04		Ke = 2.14		Ke = 4.50		Ke = 5.45		Ke = 6.76	
		Number	W	Number	W	Number	W	Number	W	Number	W	Number	W
No Wind													
0.00	0.00	1	0	18	0	35	0	52	0	69	0	86	0
Down-Estuary Wind													
−0.005	−2.35	2	−0.24	19	−0.25	36	−0.27	53	−0.26	70	−0.25	87	−0.26
−0.01	−3.20	3	−0.49	20	−0.51	37	−0.54	54	−0.52	71	−0.51	88	−0.52
−0.02	−4.34	4	−0.97	21	−1.00	38	−1.07	55	−1.06	72	−1.00	89	−1.02
−0.03	−5.17	5	−1.46	22	−1.50	39	−1.59	56	−1.57	73	−1.49	90	−1.52
−0.05	−6.41	6	−2.46	23	−2.49	40	−2.63	57	−2.64	74	−2.46	91	−2.52
−0.07	−7.37	7	−3.44	24	−3.49	41	−3.67	58	−3.71	75	−3.45	92	−3.52
−0.15	−10.03	8	−7.66	25	−7.57	42	−7.82	59	−8.02	76	−7.34	93	−7.36
−0.25	−12.27	9	−13.43	26	−13.15	43	−13.25	60	−13.42	77	−12.23	94	−12.01
Up-Estuary Wind													
0.005	2.35	10	0.26	27	0.26	44	0.27	61	0.26	78	0.25	95	0.26
0.01	3.20	11	0.52	28	0.53	45	0.56	62	0.53	79	0.51	96	0.53
0.02	4.34	12	1.04	29	1.08	46	1.13	63	1.09	80	1.03	97	1.08
0.03	5.17	13	1.56	30	1.65	47	1.72	64	1.65	81	1.54	98	1.64
0.05	6.41	14	2.56	31	2.85	48	2.98	65	2.74	82	2.61	99	2.78
0.07	7.37	15	3.57	32	4.04	49	4.34	66	3.93	83	3.73	100	3.90
0.15	10.03	16	7.45	33	8.39	50	9.56	67	9.77	84	8.69	101	9.12
0.25	12.27	17	12.32	34	13.61	51	15.49	68	16.74	85	16.14	102	17.36

[a]The wind is spatially uniform and a temporal half-sinusoidal function from day 25 to 27.5, with peak wind stress shown below. Kelvin number (Ke) is calculated using Coriolis parameter f that is 0, 25, 50, 100, 125 and 150 percent of the value for Chesapeake Bay. W is Wedderburn number. Both numbers are defined in Section 5.

variation in the along-channel direction is weak (i.e., $\partial/\partial x = 0$), we obtain the following simplifications:

$$\omega_x = -\frac{\partial v}{\partial z},\ \omega_y = \frac{\partial u}{\partial z},\ \omega_z = -\frac{\partial u}{\partial y}, \tag{4}$$

$$P = p_a + g\rho_0\eta + g\int_z^0 \rho'(z')dz', \tag{5}$$

$$\frac{\partial}{\partial y}\left(-\frac{1}{\rho}\frac{\partial P}{\partial z}\right) = \frac{\partial g}{\partial y} = 0, \tag{6}$$

$$\begin{aligned} -\frac{\partial}{\partial z}\left(-\frac{1}{\rho}\frac{\partial P}{\partial y}\right) &\approx -\frac{\partial}{\partial z}\left(-g\frac{\partial\eta}{\partial y} + \frac{g}{\rho_0}\int_0^z \frac{\partial\rho'}{\partial y}dz'\right) \\ &= -\frac{g}{\rho_0}\frac{\partial\rho'}{\partial y} \approx -g\beta\frac{\partial S}{\partial y}, \end{aligned} \tag{7}$$

in which p_a is the atmospheric pressure, g the gravitational constant, η the sea surface height, ρ' the density perturbations, and β the saline contraction coefficient. The last step in equation (7) is derived by using the linear equation of state and assuming uniform temperature in the estuary. Substituting equations (4)–(7) into equation (3) leads to

$$\frac{d\omega_x}{dt} = \underbrace{f\frac{\partial u}{\partial z}}_{\text{tilting of planetary vorticity}} \underbrace{-g\beta\frac{\partial S}{\partial y}}_{\text{baroclinicity}} + \underbrace{\frac{\partial^2}{\partial z^2}(K_V\omega_x)}_{\text{vertical diffusion}} + \underbrace{\frac{\partial^2}{\partial y^2}(K_H\omega_x)}_{\text{horizontal diffusion}}, \tag{8}$$

in which the horizontal eddy viscosity K_H is assumed to be a constant. In equation (8), the titling of planetary vorticity by shear in the along-channel flow and the baroclinicity due to the sloping isopycnals in the cross-channel sections are two terms generating the streamwise vorticity whereas the vertical and horizontal diffusion act to reduce it. The vorticity generation due to the stretching and tilting of relative vorticity is zero since $\partial/\partial x = 0$. Equation (8) can also be derived by taking $-\partial/\partial z$ of equation (2) and using the hydrostatic approximation to calculate the pressure distribution. In the ROMS model, the equations of motions are solved in a transformed coordinate system which has a generalized topography-following σ coordinate in the vertical direction and orthogonal curvilinear coordinates in the horizontal directions [*Haidvogel et al.*, 2000]. To utilize ROMS diagnostic outputs for the analysis of vorticity dynamics, we transform equation (8) into an equation in the ROMS coordinate. Please see Appendix B for details.

[12] Another goal of this paper is to examine how the wind-driven lateral circulation affects the along-channel flow. The along-channel momentum equation is given by

$$\frac{\partial u}{\partial t} = \underbrace{-\frac{1}{\rho}\frac{\partial P}{\partial x}}_{\text{pressure gradient}} + \underbrace{\frac{\partial}{\partial z}\left(K_V\frac{\partial u}{\partial z}\right)}_{\text{stress divergence}} + \underbrace{fv}_{\text{Coriolis acceleration}} - \underbrace{\left(u\frac{\partial u}{\partial x} + v\frac{\partial u}{\partial y} + w\frac{\partial u}{\partial z}\right)}_{\text{nonlinear advection}}. \tag{9}$$

The first two terms on the right-hand side of equation (9) are the pressure gradient and stress divergence. The response of an idealized rectangular estuary to axial wind-forcing is shown to consist of a vertically sheared two-layer circulation and has been interpreted in terms of the competition between the stress divergence and pressure gradient due to sea level setup [e.g., *Wang*, 1979; *Garvine*, 1985; *Janzen and Wong*, 2002]. The stress divergence overcomes the pressure

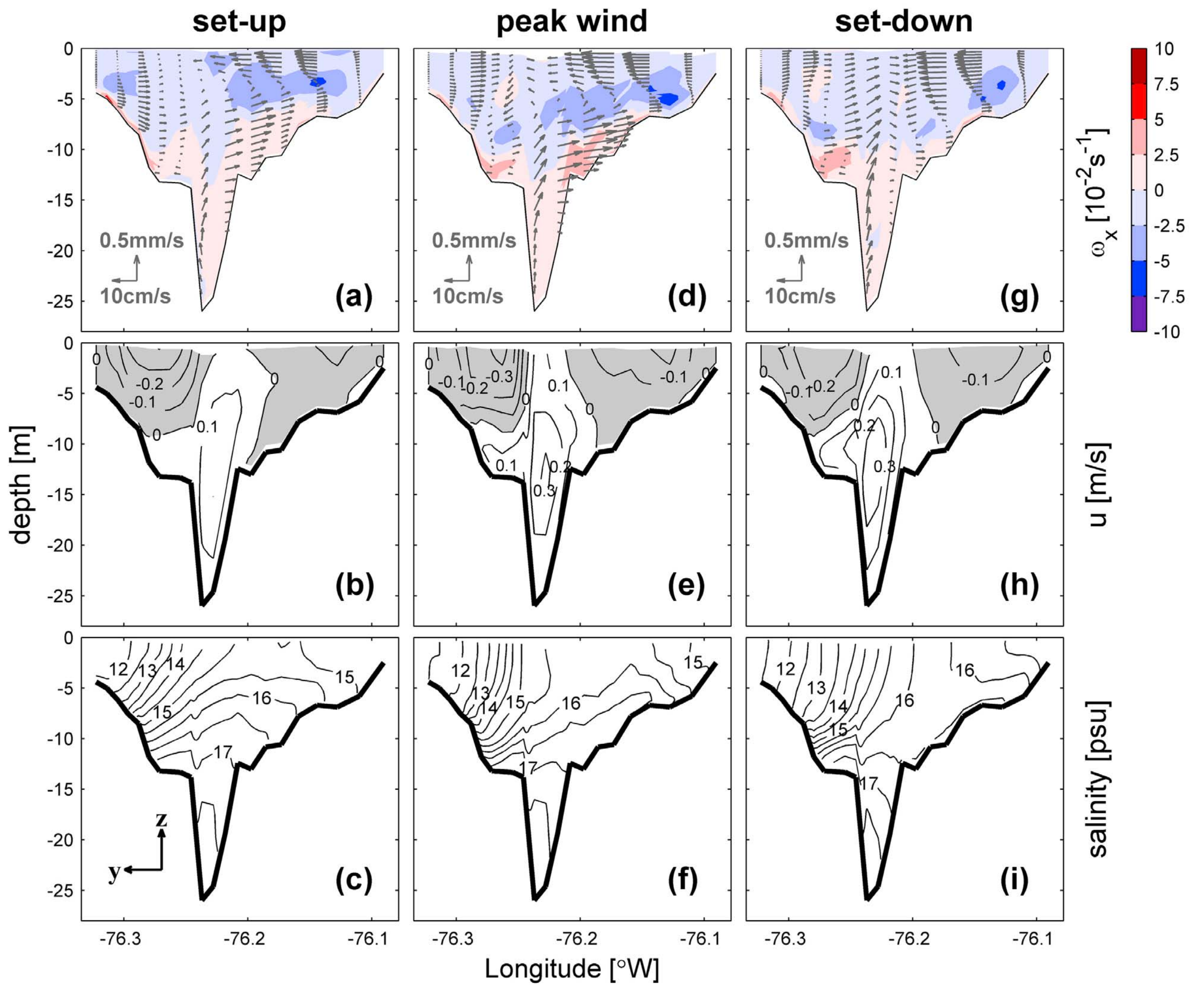

Figure 2. Temporal evolution of (a, d, and g) the streamwise vorticity (color) and the lateral-vertical velocity vectors, (b, e, and h) the along-channel velocity, and (c, f, and i) salinity at a cross-channel section under the down-estuary wind with the peak wind stress of −0.07 Pa. The snapshots are taken at 12-h into the wind event (day 25.5), peak wind (day 26.25), and 12-h toward the end of wind (day 27). The plot is looking into estuary and the positive vorticity indicates clockwise motion.

gradient to drive the downwind flow in the surface layer whereas the pressure gradient overcomes the stress divergence to drive the upwind flow in the bottom layer. If the lateral flows are strong, however, the Coriolis acceleration and nonlinear advection can also play important roles in the along-channel momentum balance. They will be investigated in this paper. Appendices A and B give details on the diagnostic analyses of the momentum and vorticity equations using ROMS model outputs.

3. Vorticity Dynamics of Lateral Circulation

[13] In Chesapeake Bay where the baroclinic Rossby radius (about 5 km) is smaller than or comparable to the width of the estuary (5–20 km), the along-channel winds can drive lateral Ekman flows and isopycnal movements, generating upwelling/downwelling at shallow shoals [*Malone et al.*, 1986; *Sanford et al.*, 1990; *Scully*, 2010]. In this section, we investigate the dynamics of wind-driven lateral circulation using the streamwise vorticity as the primary diagnostic quantity. First we show distributions of salinity, along- and cross-channel velocities at a cross-channel section, and study how they evolve during a down-/up-estuary wind event. We then examine temporal evolution of the streamwise vorticity and conduct diagnostic analysis of the vorticity equation to explore the generation mechanisms for the lateral circulation.

[14] Figure 2 shows the estuary's response to the down-estuary (southward) wind with the peak wind stress τ_p = −0.07 Pa. We apply a 34-h low-pass filter to remove tidal oscillations. The southward wind drives a westward Ekman flow (positive v) in the upper layer (about 4 m deep), which in turn drives an eastward return flow (negative v) in the lower layer. A counterclockwise circulation thus appears in the cross-channel section, with the cross-channel speed reaching about 0.1 m s^{-1} (Figure 2a). This circulation cell is

situated over the deep channel and eastern shoal, but flows on the western shoal are directed eastward where a strong lateral salinity gradient exists (Figure 2c). The southward wind drives a seaward along-channel flow (negative u) in the upper layer and a landward flow (positive u) in the lower layer, reinforcing the two-layer gravitational circulation (Figure 2b). However, the bottom return flow breaks into the surface over the center channel. The counterclockwise lateral circulation strains the salinity field and tilts the isopycnals (isohalines) toward the vertical direction, as shown in Figure 2c (see *Li and Li* [2011] for a more detailed discussion).

[15] At the peak wind, the surface Ekman layer deepens to over 5 m depth and the lateral circulation strengthens such that the maximum cross-channel velocity reaches about 0.15 m s^{-1} (Figure 2d). The along-channel current also gets stronger: both the downwind current in the upper layer and upwind current in the lower layer reach a maximum of 0.30 m s^{-1} (Figure 2e). Continued vertical tilting of isopycnals and vertical mixing almost erase stratification in the upper layer, as shown in Figure 2f. In weakly stratified water, the effects of the bottom bathymetry become important such that the along-channel flows are laterally sheared with the upwind flow in the center channel [*Csanady*, 1973; *Wong*, 1994; *Winant*, 2004]. During the set-down phase of the wind event, the counterclockwise circulation is still strong on the eastern half of the cross-section, but flows on the western half are directed eastward due to the lateral density gradients there (Figures 2g and 2i). Therefore, the wind-driven lateral circulation in a stratified estuary is not solely determined by the wind-forcing but is also affected by the cross-channel density gradient and vertical stratification.

[16] The streamwise vorticity ω_x provides a concise description of the lateral circulation, as shown in Figures 2a, 2d, and 2g. The counterclockwise lateral circulation is represented by negative values of ω_x. Strong negative vorticity emerges over the eastern half of the cross-channel section, which corresponds well with the counterclockwise circulation there. Near the bottom boundary on the shallow shoals and inside the deep channel, v slows down as the bottom is approached such that ω_x is positive. As the wind speed increases, the magnitude of ω_x becomes larger and the region of negative ω_x occupies a larger area of the water column. When the wind speed decreases, ω_x becomes weaker and the lateral circulation spins down.

[17] The sense of the lateral circulation is reversed under the up-estuary (northward) wind-forcing since the wind-driven Ekman transport is now directed eastward (Figure 3). The one-cell clockwise circulation extends over the whole cross-channel section, strengthens as the wind speed increases, and then weakens as the wind speed decreases. The cross-channel velocity v reaches a maximum speed of 0.2 m s^{-1}. Compared with counterclockwise circulation generated by the down-estuary wind, the clockwise circulation generated by the up-estuary wind is much stronger. The distribution of the streamwise vorticity ω_x also shows the asymmetry clearly: the magnitude of ω_x generated by the up-estuary wind is 2–3 times as large as that generated by the down-estuary wind. The maximum value of ω_x reaches $\sim 11 \times 10^{-2}$ s^{-1} at the peak wind. In the absence of wind-forcing, the along-channel flow features a seaward flow in a surface layer hugging the western shore and a landward flow sitting in deep channel. The up-estuary northward wind generates landward flows in the upper layer and seaward flows in the lower layer. Initially, the gravitational circulation still dominates, as shown in Figure 3b. At the peak wind, however, the wind-driven circulation reverses the gravitational circulation, with the upper layer moving up-estuary and the lower layer moving down-estuary (Figure 3e). This circulation persists and gradually weakens until the end of wind event. It should be noted that the along-channel flow generated by the up-estuary wind is about 1/3 to 1/2 of the flow generated by the down-estuary wind (compare Figures 3b, 3e, and 3h with Figures 2b, 2e, and 2h). Moreover, the vertical stratification under the up-estuary wind is significantly stronger than that under the down-estuary wind. Upwelling flows lift isopycnals on the western side up from the depressed positions (Figures 3c and 3f). Compared with the down-estuary wind case (Figures 2c and 2f), the isopycnals appear to be more horizontal, and significant stratification is retained in the top 5 m and strong Ekman flow is confined to a relatively shallow surface layer. The stratification lessens the effects of bottom bathymetry on the flow structure. Hence, the along-channel flows appear to be more vertically sheared than laterally sheared. During the second half of the wind event, the continued straining of salinity field by the clockwise circulation tilts isopycnals toward the vertical direction (Figure 3i).

[18] The above analysis suggests that the Ekman transport is the primary driving force for the lateral circulation but other factors such as the lateral density gradient and vertical stratification also play important roles in determining the strength of the lateral circulation. To gain insights into the generation mechanisms, we conduct diagnostic analysis of the streamwise vorticity equation and select the peak wind as the time slice for the analysis. The dominant terms in the vorticity budget are the titling of planetary vorticity by the shear in the along-channel flows, vertical diffusion and the baroclinicity due to sloping isopycnals in cross-channel sections. The horizontal diffusion term is two orders of magnitude smaller than the vertical diffusion term. The nonlinear advection term is weak, and the time tendency $\partial\omega_x/\partial t$ is also small (Figures 4g and 4h). Not surprisingly, the sign of the streamwise vorticity (or the sense of the lateral circulation) is set by the tilting of planetary vorticity by the along-channel current (Figures 4a and 4b). The down-estuary wind generates the southward (negative) along-channel current. The vertical shear bends f down toward the bay mouth and generates a negative streamwise vorticity. In contrast, the up-estuary wind generates the northward (positive) along-channel current which tilts f to generate positive ω_x. The turbulent diffusion acts to spin down ω_x and smooth the spatial gradients in ω_x (Figures 4c and 4d). This competition between the tilting and diffusion terms provides an interpretation of the Ekman-driven lateral circulation in unstratified channel from the vorticity point of view. In stratified estuaries such as Chesapeake Bay, the barolinicity forcing is important and is a major cause for the asymmetry in ω_x between the down-estuary and up-estuary winds. Without the wind-forcing, the brackish plume is pushed to the western shore, leading to higher sea level there. On the other hand, isopycnals are tilted downward on the western shore. Since the total pressure is the sum of the barotropic and baroclinic pressure, the isobars and isopycnals at the cross-channel

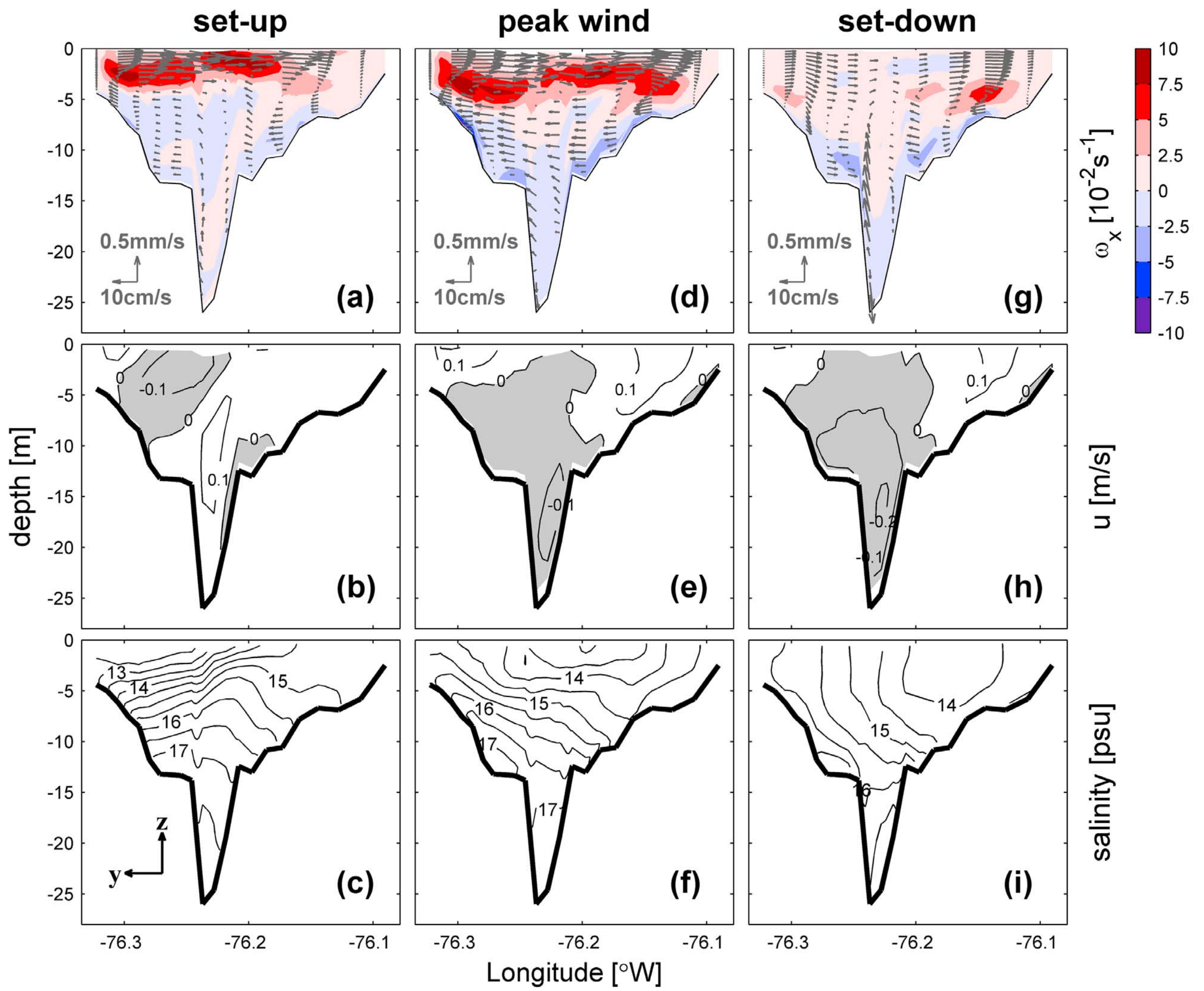

Figure 3. Temporal evolution of (a, d, and g) the streamwise vorticity (color) and the lateral-vertical velocity vectors, (b, e, and h) the along-channel velocity, and (c, f, and i) salinity at a cross-channel section under the up-estuary wind with the peak wind stress of 0.07 Pa. The snapshots are taken at 12-h into the wind event (day 25.5), peak wind (day 26.25), and 12-h toward the end of wind (day 27). The plot is looking into estuary and the positive vorticity indicates clockwise motion.

section are misaligned. The down-estuary wind steepens the slopes of the sea surface and isopycnals, particularly over the western half of the cross-channel section. Since the vertically tilted isopycnals tend to slump toward the horizontal equilibrium position, the baroclinic forcing generates positive ω_x (Figure 4e). In contrast, the up-estuary wind lifts up the isopycnals from their initial depressed positions on the western shoal (Figure 3f) such that the baroclinic forcing is relatively weaker (Figure 4f).

[19] The dynamics of the wind-driven lateral circulation can be illustrated more clearly by averaging the streamwise vorticity over a control volume (see Figure 1) and calculating the volume-averaged terms in the vorticity equation (see Appendix B). The volume-averaged $\overline{\omega_x}$ has a small value of -0.069×10^{-2} s^{-1} before the onset of wind event (Figure 5a). It spins up as the wind stress increases and spins down as the wind decreases. A large difference is found in the strength of $\overline{\omega_x}$ between the down- and up-estuary winds. $\overline{\omega_x}$ peaks at -0.54×10^{-2} s^{-1} during the down-estuary wind but at 1.32×10^{-2} s^{-1} (nearly 3 times larger) during the up-estuary wind (Figures 5a and 5c). To understand what causes such an asymmetry, we compare the volume-averaged terms in the vorticity equation. Before the onset of wind-forcing, the tilting of planetary vorticity $\overline{f\frac{\partial u}{\partial z}}$ (negative) is balanced by the baroclinic forcing $\overline{-g\beta\frac{\partial S}{\partial y}}$ (positive), i.e., the along-channel flow is in thermal wind balance with the lateral density gradient. This balance is disrupted by the wind-forcing, particularly during the up-estuary wind. The down-estuary wind amplifies the two-layer gravitational circulation so that $\overline{f\frac{\partial u}{\partial z}}$ doubles (Figure 5b). In contrast, the up-estuary wind generates a two-layer baroclinic current that opposes the gravitational circulation. The shear in the along-channel current is negative initially but turns to be positive as the up-estuary wind reverses the gravitational circulation (landward

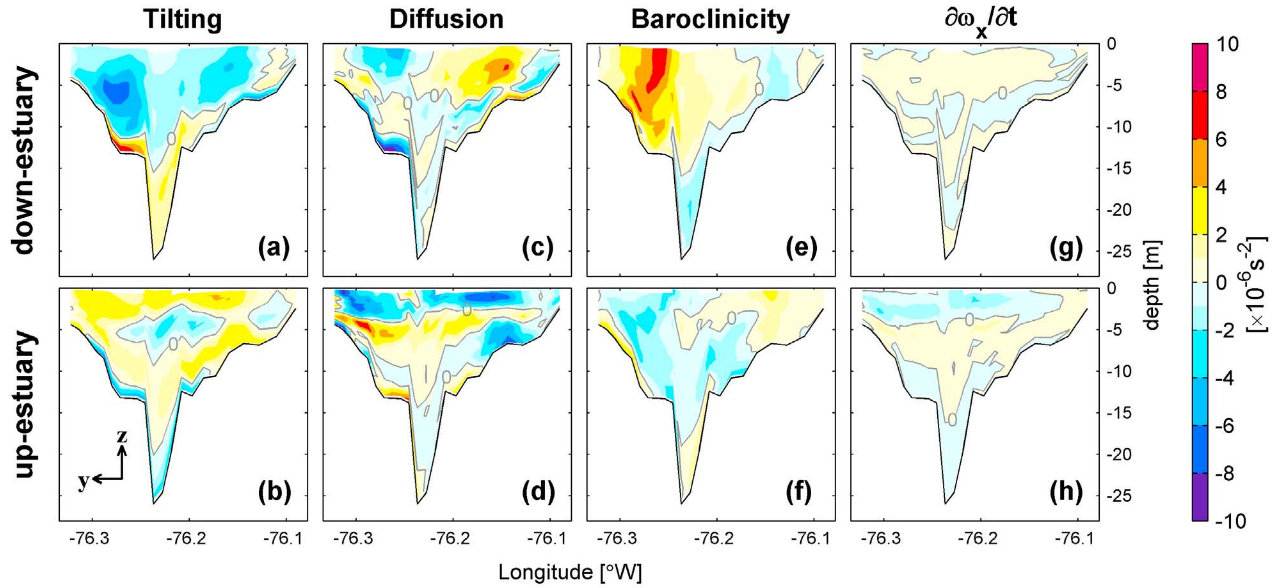

Figure 4. Terms in the streamwise-vorticity equation: (a and b) the tilting of planetary vorticity, (c and d) turbulent diffusion, (e and f) baroclinicity, and (g and h) time tendency under the down- and up-estuary wind with the peak magnitude of 0.07 Pa. The snapshots are taken at the peak of wind event. The cross-section is looking into estuary, and positive values indicate clockwise rotation. The unit of vorticity terms is 10^{-6} s^{-2}.

in the upper layer and seaward in the lower layer). Consequently $\overline{f \frac{\partial u}{\partial z}}$ is initially negative but becomes positive later (Figure 5d). It should be noted that $\overline{f \frac{\partial u}{\partial z}}$ shows much larger departure from its pre-wind value during the up-estuary wind than during the down-estuary wind. While the tilting of planetary vorticity acts as a source for ω_x, the turbulent diffusion acts as a sink to spin down ω_x. The two terms are nearly 180° out of phase during the wind event. Due to the lateral straining of isopycnals, the eddy viscosity is 1.2×10^{-3} m^2 s^{-1}, about 37% smaller than 1.9×10^{-3} m^2 s^{-1}

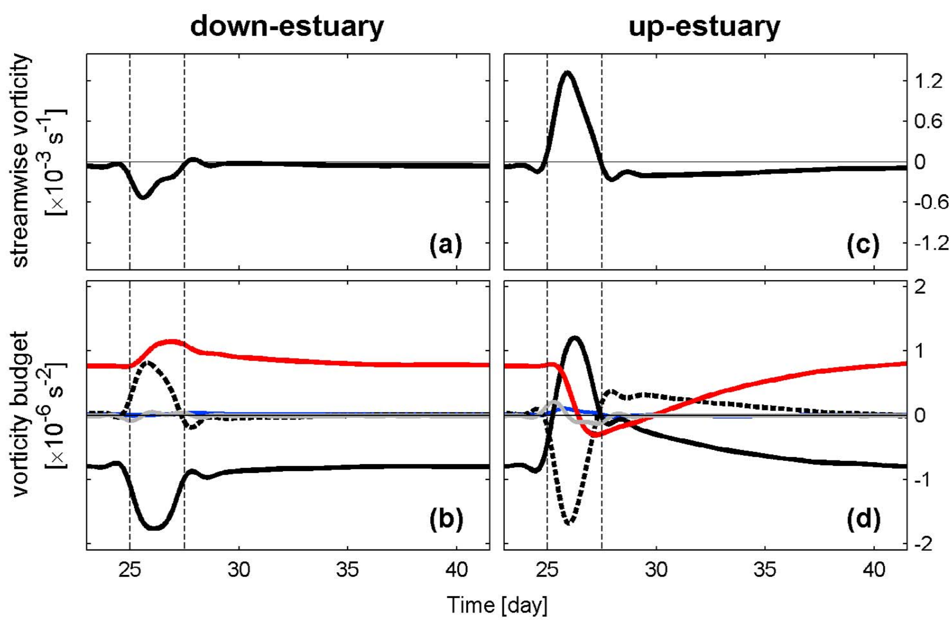

Figure 5. Time series of the volume-averaged (a and c) streamwise vorticity ($\overline{\omega_x}$) and (b and d) the terms in the vorticity equation: the tilting of planetary vorticity f (black solid), turbulent diffusion (black dashed), baroclinicity (red), nonlinear advection (blue) and time change rate (gray) under the down- and up-estuary wind with the peak magnitude of 0.07 Pa.

during down-estuary wind. However, the vertical gradient of ω_x is much larger during the up-estuary wind. The net result is that the turbulent diffusion of ω_x is much stronger during the up-estuary wind than during the down-estuary wind. As shown in Figure 5, the time series of the volume-averaged diffusion appears to be a mirror image of the perturbation of $\overline{f\frac{\partial u}{\partial z}}$ from its pre-wind value. This reveals a counter-balance between the vorticity generation due to the titling of the planetary vorticity and the vorticity destruction due to the turbulent diffusion. In comparison to the two terms, the nonlinear advection term is small enough to be neglected (Figures 5b and 5d).

[20] The baroclinic forcing is elevated during the down-estuary wind since the counterclockwise circulation tilts the isopycnals toward the vertical direction and amplifies $\overline{-g\beta\frac{\partial S}{\partial y}}$. A more dramatic effect is noted during the up-estuary wind when $\overline{-g\beta\frac{\partial S}{\partial y}}$ initially helps to generate the clockwise lateral circulation but reduces to near zero values as the isopycnals slump back to horizontal equilibrium positions. During the second half of the up-estuary wind event, continual upwelling on the western shoal lifts high salinity bottom water to the surface and creates a negative baroclinic forcing, but $\overline{-g\beta\frac{\partial S}{\partial y}}$ is relatively weak since the isopycnals are widely spaced (see Figure 3i).

[21] The feedback mechanisms between the baroclinicity and lateral Ekman flows are different under the down- and up-estuary winds. When the estuary is forced by the down-estuary wind, the vertical shear in the along-channel current results in a negative vorticity ($f\frac{\partial u}{\partial z} < 0$), but the counterclockwise lateral circulation steepens the isopycnals, leading to a positive vorticity ($-g\beta\frac{\partial S}{\partial y} > 0$). A negative feedback thus exists to weaken the lateral circulation. When the estuary is forced by the up-estuary wind, however, the along-channel shear is reversed so that the positive streamwise vorticity ($f\frac{\partial u}{\partial z} > 0$) is produced. During the first half of the wind event, the baroclinic forcing $-g\beta\frac{\partial S}{\partial y} > 0$ contributes to the generation of the positive streamwise vorticity but weakens as the isopycnals are flattened. Further straining of the density field by the clockwise circulation leads to a weak baroclinic forcing $-g\beta\frac{\partial S}{\partial y} < 0$ that opposes $f\frac{\partial u}{\partial z} > 0$. When integrated over the whole wind event, the baroclinic forcing is positive under both the down- and up-estuary winds, and contributes to the generation of positive streamwise vorticity and clockwise lateral circulation.

4. Effects on the Along-Channel Flow

[22] In tidally driven estuaries, recent studies have shown that nonlinear advection by lateral flows is of the first order of importance in the subtidal along-channel momentum balance and acts as a driving force for the estuarine exchange flows [*Lerczak and Geyer*, 2004; *Scully et al.*, 2009]. In this section we investigate how the wind-driven lateral circulation affects the along-channel flow.

[23] Figure 6 shows a comparison of the along-channel and cross-channel velocities among three runs: (1) down-estuary wind; (2) no-wind; (3) up-estuary wind. Without wind-forcing, the estuary is characterized by a two-layer residual gravitational circulation with speeds reaching 0.1 m s^{-1}, as shown in the along-channel distribution of the along-channel velocity (Figure 6b). The lateral flows are weak and generated by the interaction between moderate tidal currents and density field (Figure 6e). When the down-estuary wind is applied over the Bay, it drives a seaward-directed current in the upper layer and a return flow in the lower layer, thus amplifying the gravitational circulation in the along-channel section (Figure 6a). A counterclockwise lateral circulation develops in the cross-channel section (Figure 6d). When the wind blows up-estuary, it drives a two-layer circulation that opposes the gravitational circulation (Figure 6c). At the peak wind, the wind-driven circulation nearly cancels the gravitational circulation so that the along-channel flows are weak. In the meantime, a strong clockwise lateral circulation develops in the cross-channel section, with speeds comparable to the along-channel currents (Figure 6f).

[24] To determine if the lateral circulation affects the along-channel flow, we conduct a diagnostic analysis of the along-channel momentum equation (equation (9)), as shown in Figure 7. Both the down-estuary and up-estuary cases are considered and the time slice is selected at 12 h into the wind event. The stress divergence $\frac{\partial}{\partial z}\left(K_V\frac{\partial u}{\partial z}\right)$ and longitudinal pressure gradient $-\frac{1}{\rho}\frac{\partial P}{\partial x}$ are two leading terms in the momentum equation. It is interesting to note that the Coriolis force *fv* exhibits a two-layer structure over the cross-channel section. Under the down-estuary wind, the stress divergence overcomes the pressure gradient to drive a downwind flow in the upper layer. In the lower layer, the pressure gradient overpowers the stress divergence to drive an upwind flow (Figures 7a and 7c). The Coriolis acceleration *fv* has the opposite sign to the stress divergence in the upper layer and the opposite sign to the pressure gradient in the lower layer (Figure 7e). Hence it weakens the downwind current in the upper layer and the upwind current in the lower layer, thereby reducing the shear in the along-channel current. The same result applies to the up-estuary wind (Figures 7b, 7d, and 7f). Figure 8 is a schematic diagram that illustrates how the Coriolis acceleration on the lateral flows weakens the shear in the along-channel currents under both down- and up-estuary winds.

[25] The nonlinear advection term $-\left(u\frac{\partial u}{\partial x} + v\frac{\partial u}{\partial y} + w\frac{\partial u}{\partial z}\right)$ shows complex spatial patterns due to flow-topography interactions but is generally smaller than the Coriolis term (Figures 7g and 7h). It has no obvious correlation with other terms in the momentum equation. Although the nonlinear advection by tidally driven lateral circulation has been found to play a significant role in driving the along-channel estuarine exchange flows, we find that the nonlinear advection by wind-driven lateral circulation does not play a coherent role in driving the along-channel flows.

[26] The above analysis is limited to a mid-bay cross-section at one time snapshot. In order to compare the magnitudes of each term in the along-channel momentum equation for the whole Bay, we calculate the volume-averaged quantities for the upper and lower layers. Since $\frac{\partial}{\partial z}\left(K_V\frac{\partial u}{\partial z}\right)$ switches sign at a depth of around 5 m (see Figure 7), we define fixed volumes for the upper and lower layers by separating them at this depth. The time series of the layer-averaged terms are shown in Figure 9. We experiment with other ways for the volume integration (e.g., chose a separation depth at 7 m) and obtain the same results.

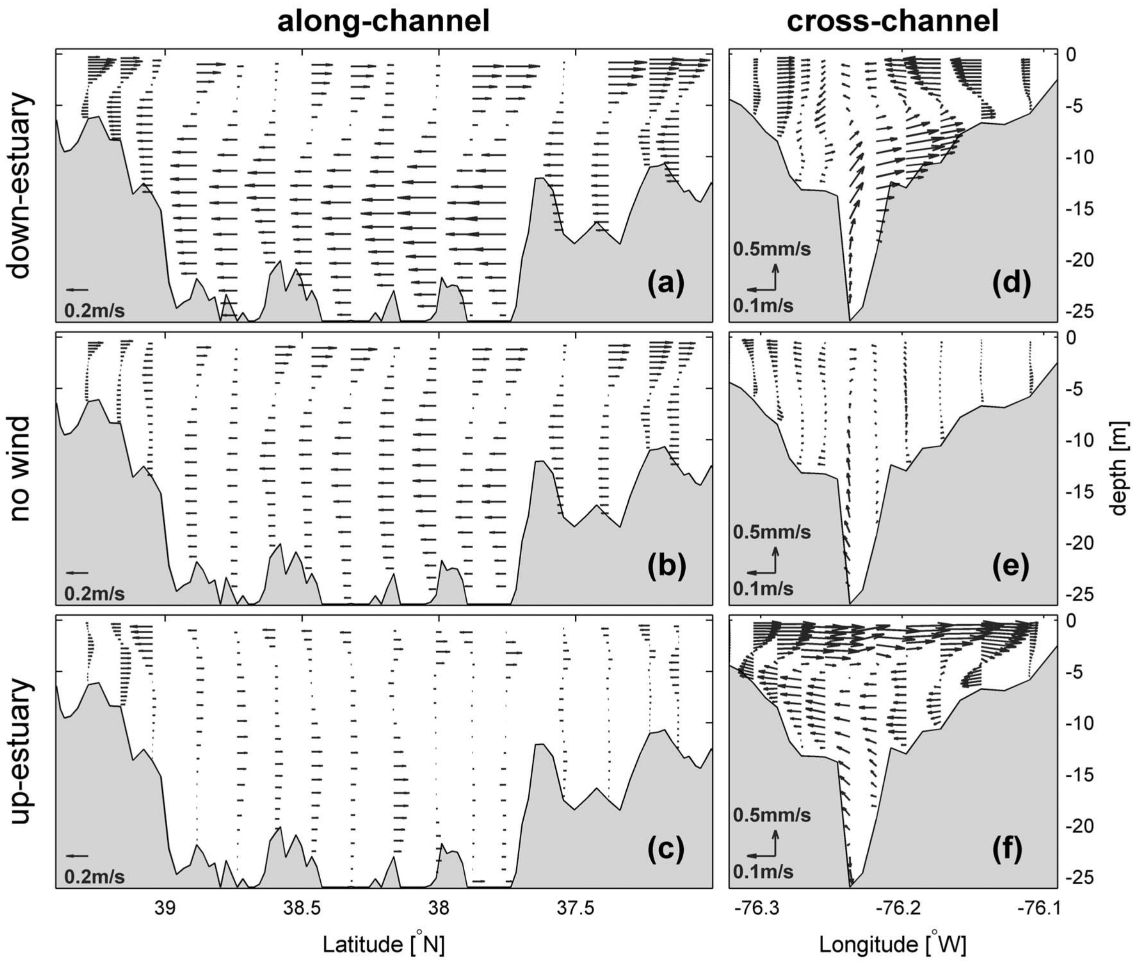

Figure 6. Distributions of (a–c) the subtidal along-channel current in the along-channel section and (d–f) velocity vectors at a cross-channel section for three model runs: down-estuary wind (Figures 6a and 6d); no wind (Figures 6b and 6e) and up-estuary wind (Figures 6c and 6f). The snapshots are taken on 26.25 day when the wind stress reaches the peak magnitude of 0.07 Pa in the two wind runs.

[27] First we study the down-estuary wind. For the upper layer, the stress divergence overcomes the along-channel pressure gradient to produce a negative value (with a maximum of -3.59×10^{-6} m s^{-2}) which drives the seaward flow. The Coriolis force acting the westward flows counteracts the stress divergence (with a maximum of 2.56×10^{-6} m s^{-2}) (Figure 9a). The nonlinear advection also slightly opposes the stress divergence term, but does not change much with time. The local acceleration is relatively small and its sign change during the wind event is consistent with the temporal development of the along-channel current. In the lower layer, the longitudinal pressure gradient overpowers the stress divergence to generate positive value (with a maximum of 2.36×10^{-6} m s^{-2}) and landward return flow whereas $fv < 0$ (with a maximum of -1.66×10^{-6} m s^{-2}). Once again the Coriolis term associated with the lateral flow opposes the pressure gradient that drives landward flow in the lower layer (Figure 9b).

[28] Under the up-estuary wind, the imbalance between $-\frac{1}{\rho}\frac{\partial P}{\partial x}$ and $\frac{\partial}{\partial z}\left(K_V \frac{\partial u}{\partial z}\right)$ is much larger, reaching a maximum of 4.20×10^{-6} m s^{-2} in the upper layer and a minimum of -4.39×10^{-6} m s^{-2} in the lower layer. Since the lateral circulation is 2–3 times stronger under the up-estuary wind, fv is much larger, reaching a minimum of -3.84×10^{-6} m s^{-2} in the surface layer and a maximum of 3.13×10^{-6} m s^{-2} in the bottom layer. The nonlinear advection term plays a smaller role in the along-channel momentum balance under the up-estuary wind, as shown in Figures 7g and 7h.

5. Regime Diagrams

[29] In the last two sections, we conducted detailed analysis of the lateral circulation dynamics under one representative wind stress of $|\tau_p|$ = 0.07 Pa (or wind speed of about 7.4 m s^{-1}). Now we investigate how the lateral circulation and along-channel current shear vary with the wind speed. Figure 10 shows the time series of the volume-averaged streamwise vorticity $\overline{\omega_x}$ for a wide range of wind stress (or speed) magnitudes. For all the winds considered, the magnitude of $\overline{\omega_x}$ is much larger during the up-estuary winds than during the down-estuary winds. Under the up-estuary winds, the peak value of $\overline{\omega_x}$ increases as the peak wind stress $|\tau_p|$ increases from 0.01 to 0.15 Pa but decreases

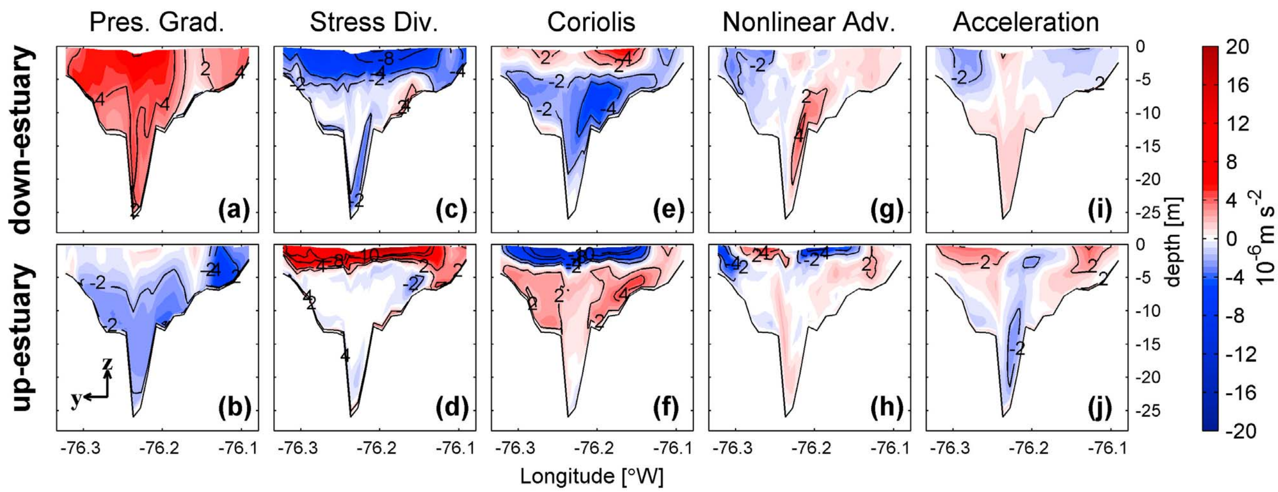

Figure 7. Distributions of the dominant terms in the subtidal along-channel momentum equation at a cross-channel section: (a and b) pressure gradient, (c and d) stress divergence, (e and f) Coriolis acceleration, (g and h) nonlinear advection, and (i and j) local acceleration. Figures 7a, 7c, 7e, 7g, and 7i are for the down-estuary run and Figures 7b, 7d, 7f, 7h, and 7j are for the up-estuary run. The snapshots are taken at 12 h into the wind event with the peak magnitude of 0.07 Pa.

slightly as $|\tau_p|$ increases further to 0.25 Pa. In contrast, the peak value of $\overline{\omega_x}$ only exhibits modest increases as $|\tau_p|$ increases from 0.01 to 0.25 Pa. It is worth noting that at high winds $\overline{\omega_x}$ peaks earlier and decreases more rapidly with time. An analysis of the streamwise vorticity budget (as in Figure 5) shows that both $f\frac{\partial u}{\partial z}$ and diffusion terms reach their maxima before the peak wind speed and suggests that strong turbulent dissipation at high winds causes a rapid

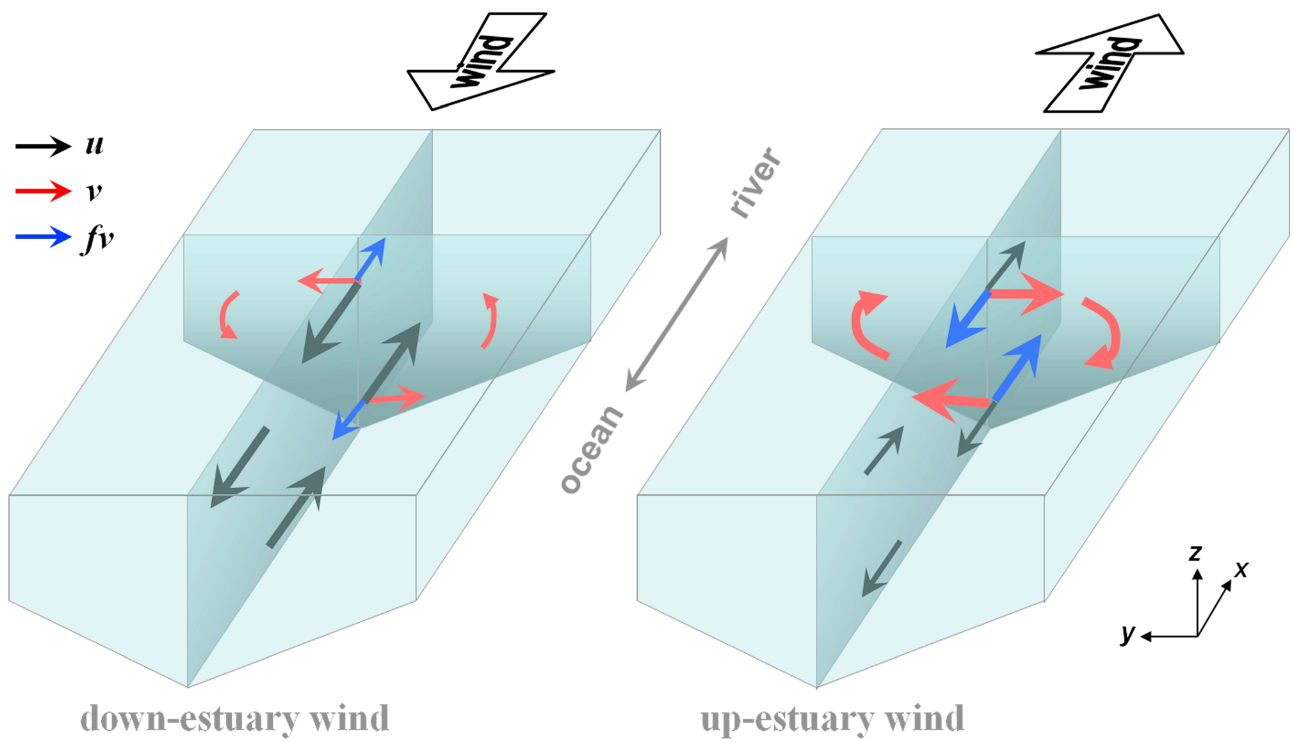

Figure 8. Conceptual diagram to illustrate the effects of Coriolis acceleration (*fv*, in blue) on the along-channel currents (*u*, in black). The lateral circulation is marked by red lines. The down-estuary wind generates seaward flow in the upper layer and landward flow in the lower layer, but the Coriolis force on the counterclockwise lateral circulation weakens this two-layer flow. The up-estuary wind generates landward flow in the upper layer and seaward flow in the lower layer, but the Coriolis force on the clockwise lateral circulation opposes this reversed two-layer flow.

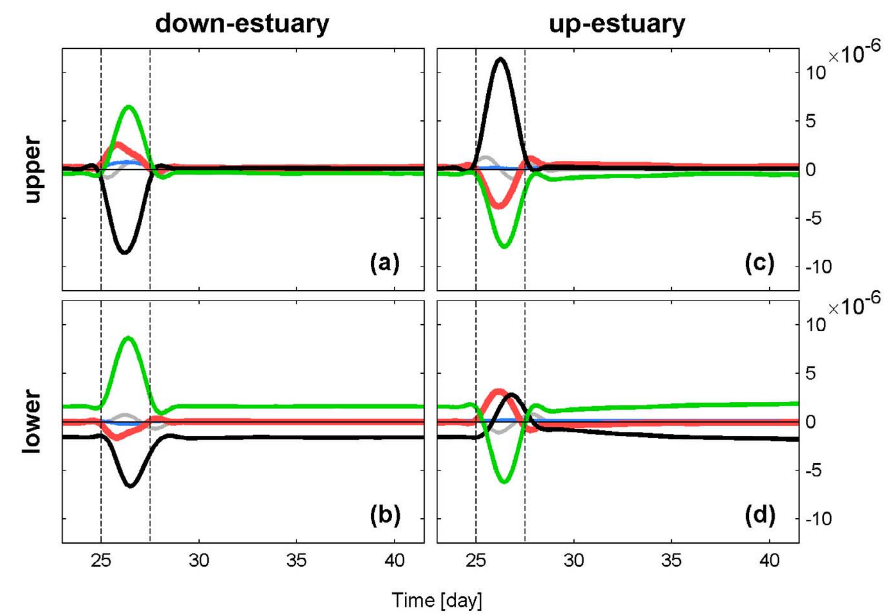

Figure 9. Integrated subtidal along-channel momentum balance for the upper and lower layers. The terms are the along-channel pressure gradient $-P_x/\rho_0$ (green), stress divergence $K_v v_{zz}$ (black), the Coriolis force fv (red), the nonlinear advection $-(uu_x + vu_y + wu_z)$ (blue), and local acceleration u_t (gray). The terms are averaged over the upper (≤5 m) and lower (>5 m) layers and in unit of m s^{-2}. (a and b) The down-estuary and (c and d) the up-estuary cases are shown. The peak magnitude of the wind is 0.07 Pa.

spin-down of the streamwise vorticity. As a result, the time average of $\overline{\omega_x}$ over the entire wind event is smaller at high winds than at intermediate wind speeds.

[30] Following *Li and Li* [2011], we summarize the model results in terms of two dimensionless parameters: Wedderburn number W and Kelvin number Ke. W is defined as

$$W = \frac{\tau_W L}{\Delta\rho g H^2}, \quad (10)$$

where L is the length of an estuary, $\Delta\rho$ the horizontal density difference, g the gravitational acceleration, and H the mean water depth [*Monismith*, 1986; *Geyer*, 1997; *Chen and Sanford*, 2009]. The Wedderburn number compares the wind-forcing with the horizontal baroclinic pressure gradient. The Kelvin number is defined as

$$Ke = \frac{fB}{\sqrt{g' h_S}}, \quad (11)$$

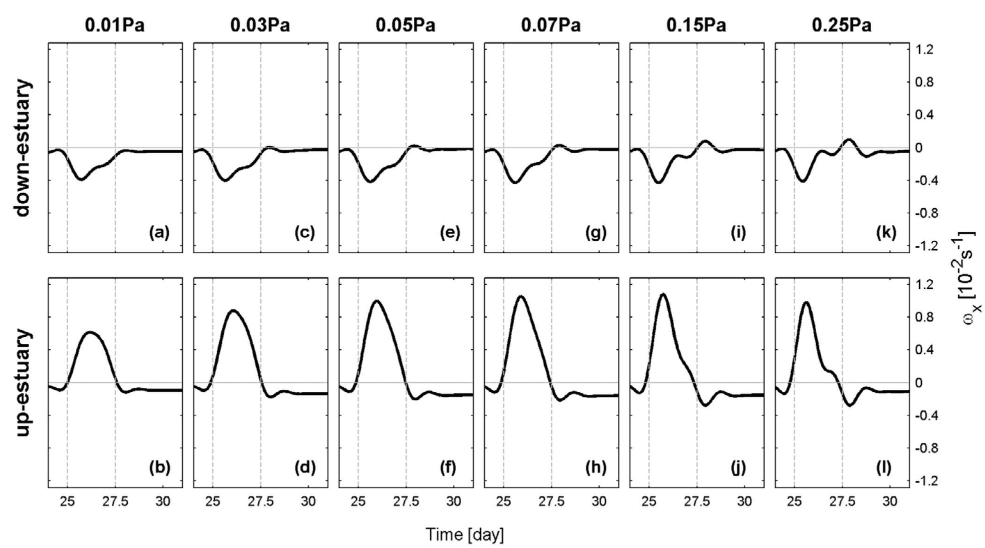

Figure 10. Time series of the volume-averaged streamwise vorticity in Chesapeake Bay at different wind stress magnitudes: (a, c, e, g, i, and k) down-estuary winds and (b, d, f, h, j, and l) up-estuary winds. The two dashed lines mark the wind event.

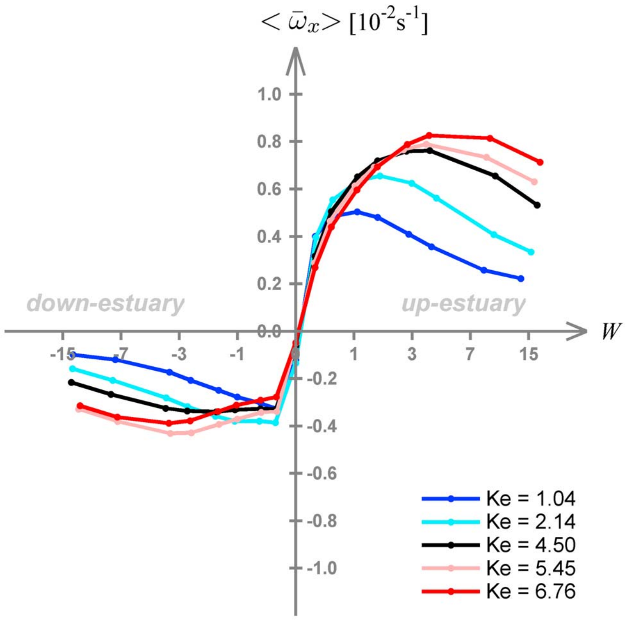

Figure 11. The volume-averaged streamwise vorticity $\langle\bar{\omega}_x\rangle$ as a function of Wedderburn (W) and Kelvin (Ke) numbers. Positive $\langle\bar{\omega}_x\rangle$ indicates the clockwise circulation. The W-axis is plotted in logarithmic scale with $\log_2(|W| + 1)$ to reveal rapid changes of $\langle\bar{\omega}_x\rangle$ at low $|W|$ values.

where f is the Coriolis parameter, B the estuary width, g' the reduced gravitational acceleration determined by the density difference between the upper and lower layers, and h_S the mean depth of the upper layer. The Kelvin number is the ratio of the estuary width to the internal Rossby radius of deformation [e.g., *Garvine*, 1995; *Valle-Levinson*, 2008]. For Chesapeake Bay, W varies from $\sim$1 to 10 for wind speeds ranging 5 $\sim$ 10 m s^{-1} and Ke = 4.5. Although the model bathymetry is specific to Chesapeake Bay, we conduct numerical experiments by varying f over a range from 25%f to 150%f to explore estuaries of different widths. Table 1 summarizes all the numerical runs we have conducted.

[31] Figure 11 shows how the time average of the streamwise vorticity $\langle\bar{\omega}_x\rangle$ over the entire wind event varies with the Wedderburn and Kelvin numbers. $\langle\bar{\omega}_x\rangle > 0$ (clockwise circulation) is for the up-estuary winds and $\langle\bar{\omega}_x\rangle < 0$ (counter-clockwise circulation) is for the down-estuary winds. At a given value of Ke, $\langle\bar{\omega}_x\rangle$ increases rapidly with increasing $|W|$ at small values of $|W|$: the lateral circulation becomes stronger as the wind-forcing gets stronger. $\langle\bar{\omega}_x\rangle$ reaches a maximum value at an intermediate value of $|W|$. At larger $|W|$, $\langle\bar{\omega}_x\rangle$ decreases since the strong dissipation at high wind speeds causes a more rapid spin-down of the streamwise vorticity. As the lateral circulation is primarily driven by the wind-induced Ekman transport, it is not surprising that $\langle\bar{\omega}_x\rangle$ increases with increasing Ke: the lateral circulation is stronger at higher latitudes or in wider estuaries. It is important to note the asymmetry in $\langle\bar{\omega}_x\rangle$ between the down- and up-estuary winds. At Ke = 4.5 (at the latitude of Chesapeake Bay), $\langle\bar{\omega}_x\rangle$ generated by the up-estuary winds is 2 times as large as that generated by the down-estuary winds.

[32] To better understand the variation of $\langle\bar{\omega}_x\rangle$ with W and Ke, we conduct a diagnostic analysis of the streamwise vorticity budget for all the model runs and plot the three leading terms in Figure 12. We average the terms over the entire wind event to show the integrated effects. The tilting of planetary vorticity by the along-channel current $\left\langle \overline{f\frac{\partial u}{\partial z}} \right\rangle$ increases with both $|W|$ and Ke. As expected, the generation of the streamwise vorticity is stronger in a strongly rotating system or at higher winds. The turbulent diffusion acts in direct opposition to $\left\langle \overline{f\frac{\partial u}{\partial z}} \right\rangle$ and shows similar variation with $|W|$ and Ke. While the tilting term tends to generate the lateral torque, the turbulent diffusion term tends to spin it down. The time-averaged baroclinic forcing term is positive during both the

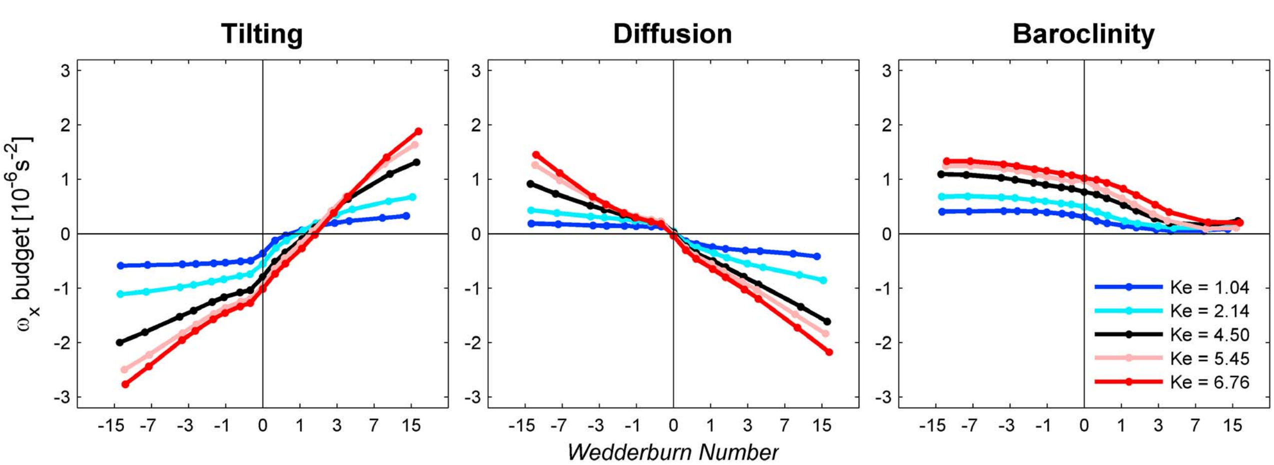

Figure 12. The volume-averaged terms in the streamwise vorticity as a function of Wedderburn (W) and Kelvin (Ke) numbers for all runs. The quantities are averaged over the whole wind event and in unit of 10^{-6} s^{-2}. Positive values correspond to the generation of clockwise circulation. $W > 0$ corresponds to the up-estuary winds whereas $W < 0$ corresponds to the down-estuary winds.

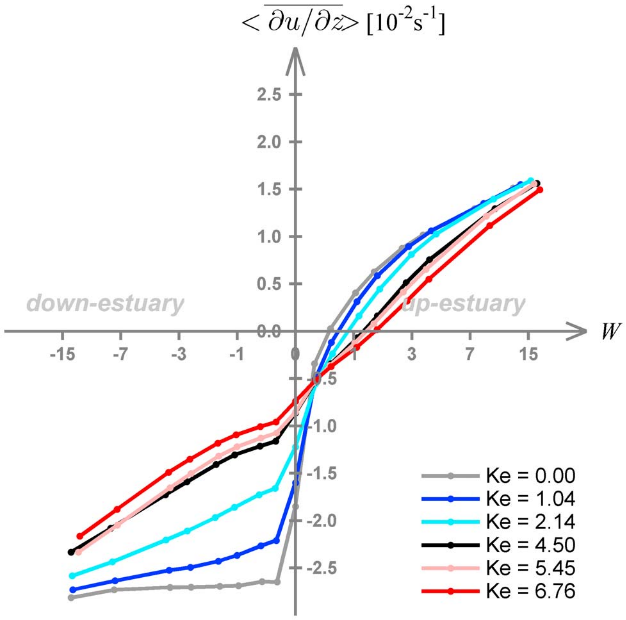

Figure 13. The volume-averaged along-channel shear $\left\langle\overline{\partial u/\partial z}\right\rangle$ as a function of Wedderburn (W) and Kelvin (Ke) numbers. Negative $\left\langle\overline{\partial u/\partial z}\right\rangle$ corresponds to the seaward flow in the upper layer and the landward flow in the lower layer.

down-estuary and up-estuary wind events. However, it is much larger during the down-estuary winds. This difference in the baroclinic forcing $\left\langle\overline{-g\beta\frac{\partial S}{\partial y}}\right\rangle$ is the main cause for the asymmetry in the strength of the lateral circulation between the down- and up-estuary winds. It is interesting to note that $\left\langle\overline{-g\beta\frac{\partial S}{\partial y}}\right\rangle$ approaches to constant (saturating) values at large values of $|W|$ for a given value of Ke. The lateral straining can only tilt the isopycnals toward the vertical directions and the lateral salinity gradient cannot increase further at higher wind speeds.

[33] In Figure 13 we examine how the time average of the along-channel current $\left\langle\overline{\frac{\partial u}{\partial z}}\right\rangle$ over the entire wind event varies with W and Ke. $Ke = 0$ corresponds to the non-rotating runs. At $W = 0$ the along-channel shear is generated by the gravitational circulation and is negative. The down-estuary winds amplify this shear. The up-estuary winds generate a two-layer baroclinic current which opposes the gravitational circulation. At low wind speeds, $\left\langle\overline{\frac{\partial u}{\partial z}}\right\rangle$ remains to be negative but turns to be positive (as the wind-driven circulation reverses the gravitational circulation) when W exceeds a threshold value. Compared with the rotating runs at the same value of W, the shear in the along-channel current is strongest in the non-rotating runs. As discussed in section 4, the Coriolis force acting on the lateral flows reduces the shear in the along-channel current. At $Ke = 4.5$ (the latitude of Chesapeake Bay), $\left\langle\overline{\frac{\partial u}{\partial z}}\right\rangle$ is about 30–40% smaller than that in runs in which the effects of the earth's rotation are not considered. The reduction in the along-channel shear is higher at higher latitudes and wide estuaries (larger values of Ke) but lower at lower latitudes and narrow estuaries.

6. Conclusions

[34] Using a numerical model of Chesapeake Bay, we have investigated the dynamics of wind-driven lateral and along-channel currents in a stratified rotating estuary. The Ekman transport associated with the along-channel winds generates a counterclockwise lateral circulation under the down-estuary winds and a clockwise lateral circulation under the up-estuary winds. However, the strength of the lateral circulation is about 2 times stronger during the up-estuary winds than during the down-estuary winds. To understand what causes this asymmetry, we have developed a new approach by conducting diagnostic analysis of the streamwise vorticity equation. It reveals a primary balance among three leading terms: the titling of the planetary vorticity by the shear in the along-channel current, the baroclinic forcing due to sloping isopycnals at cross-channel sections, and turbulent diffusion. Although the turbulent diffusion always acts to spin down the vorticity generated by the titling of the planetary vorticity, the baroclinic forcing is highly asymmetric between the down- and up-estuary winds. The counterclockwise lateral circulation generated by the down-estuary winds tilts the isopycnals toward the vertical directions and creates adverse lateral barolinic pressure gradient to hamper the lateral Ekman transport. In contrast, the clockwise lateral circulation generated by the up-estuary winds initially flattens the isopycnals and the baroclinic forcing reinforces the lateral Ekman transport.

[35] The analysis based on the streamwise vorticity could be extended to study lateral circulations in tidally forced estuaries. In the streamwise vorticity equation, the two-cell lateral circulation generated by differential advection can be described by the baroclinic forcing term $-g\beta\frac{\partial S}{\partial y}$ due to the lateral density gradient while the one-cell lateral circulation generated by the tidal rectification of lateral Ekman flow can be described by the titling of the planetary vorticity by the shear in the tidal current $f\frac{\partial u}{\partial z}$. An outstanding question is how the two mechanisms contribute to the generation of the lateral circulations in estuaries of different widths and under different river discharge and tidal forcing conditions.

[36] Previous studies of lateral circulations in narrow estuaries have shown that the nonlinear advection $-\left(u\frac{\partial u}{\partial x}+v\frac{\partial u}{\partial y}+w\frac{\partial u}{\partial z}\right)$ associated with the lateral flows works in concert with the along-channel baroclinic pressure gradient to amplify the estuarine exchange flows. In a wide estuary such as Chesapeake Bay, however, we have found that the Coriolis acceleration fv associated with the lateral flows reduces the shear in the along-channel currents. Compared with the non-rotating system, the shear reduction is about 30–40%. Future work is needed to examine the relative roles of the nonlinear advection and Coriolis acceleration in both tidally and wind-driven flows and for estuaries of different widths. In an effort to generalize the model results specific to Chesapeake Bay, we have conducted model runs by varying the Coriolis parameter f. Regime diagrams have been constructed to show how the averaged streamwise vorticity and along-channel current shear vary with the Wedderburn (W) and Kelvin (Ke) numbers. In the

future we plan to conduct model runs of an idealized generic estuary and examine how the lateral circulation and along-channel exchange flow vary in the nondimensional parameter space.

[37] The results presented in this paper are based on the outputs from a numerical model. Although this model has been validated against the observational data, there are to our knowledge no existing data with adequate temporal and spatial resolution to resolve the full three-dimensional structure of flow and density fields. Given the physical and ecological importance of the lateral circulations, especially for long estuary with wide channels, future observational study of the wind effects on lateral circulations is warranted.

Appendix A: Decomposition of Vectors Into Along- and Cross-Channel Directions

[38] We choose the along-channel direction to be aligned with the semi-major axis of the depth-averaged tidal current ellipse associated with the dominant tidal harmonics M_2. It is positive when pointing into the estuary. The cross-channel direction is defined to be at 90 degree to the along-channel direction. At each model grid point, the along- and cross-channel components of the horizontal velocity vector are calculated using the following formulae:

$$\tilde{u} = u_R \cos\theta + v_R \sin\theta, \tag{A1}$$

$$\tilde{v} = -u_R \sin\theta + v_R \cos\theta, \tag{A2}$$

where $(\tilde{u}, \tilde{v})$ are the velocity components in the along- and cross-channel directions $(\tilde{x},\tilde{y})$, (u_R,v_R) are the velocity components in the (ξ, η) directions defined in the ROMS model, and θ is the angle between the along-channel direction and the ξ-direction.

[39] To project the momentum equations into the along- and cross-channel directions, we treat each term in the momentum equation as a vector with components in the (ξ, η) directions and then apply the same decomposition as (A1)–(A2). If (ξ, η) are curvilinear coordinates, terms in the momentum equations involve coefficients related to the coordinate transformation [*Haidvogel et al.*, 2000], but the projection into the along- and cross-channel directions can be treated in the same way.

Appendix B: Calculation of Streamwise Vorticity

[40] In the Cartesian coordinate, the cross-channel momentum equation is given by

$$\frac{\partial v}{\partial t} = -fu - \frac{1}{\rho}\frac{\partial P}{\partial y} - \left(u\frac{\partial v}{\partial x} + v\frac{\partial v}{\partial y} + w\frac{\partial v}{\partial z}\right) + \frac{\partial}{\partial z}\left(K_V\frac{\partial v}{\partial z}\right) + \frac{\partial}{\partial x}\left(K_H\frac{\partial v}{\partial x}\right) + \frac{\partial}{\partial y}\left(K_H\frac{\partial v}{\partial y}\right), \tag{B1}$$

where (u, v, w) are the velocity components in the along-channel, cross-channel and vertical directions, f the Coriolis parameter, P the total pressure, and K_v and K_H are the vertical and horizontal eddy viscosities. As shown in Section 2, taking $-\partial/\partial z$ of equation (B1) yields the equation for the streamwise vorticity.

[41] In the ROMS model, the equations of motions are solved in a transformed coordinate system which has a generalized topography-following σ coordinate in the vertical direction and orthogonal curvilinear (ξ, η) coordinates in the horizontal directions [*Haidvogel et al.*, 2000]. After the decomposition into the along- and cross-channel directions $(\tilde{x},\tilde{y})$, the cross-channel momentum equation in the transformed coordinates can be written as

$$\overbrace{\frac{\partial \tilde{v}}{\partial t}}^{\text{accel}} = \overbrace{-f\tilde{u}}^{\text{cor}} + \overbrace{\left(-\frac{1}{\rho}\frac{\partial P}{\partial \tilde{y}} - \frac{g\rho}{\rho_0}\frac{\partial z}{\partial \tilde{y}}\right)}^{\text{prsgrd}} + \overbrace{\left(-\frac{\partial \tilde{u}\tilde{v}}{\partial \tilde{x}} - \frac{\partial \tilde{v}\tilde{v}}{\partial \tilde{y}} + CT\right)}^{\text{hadv}} + \overbrace{\left(-\frac{1}{H_Z}\frac{\partial H_Z \tilde{v}\Omega}{\partial \sigma}\right)}^{\text{vadv}} + \underbrace{\frac{1}{H_Z}\frac{\partial}{\partial \sigma}\left(\frac{K_V}{H_Z}\frac{\partial \tilde{v}}{\partial \sigma}\right)}_{\text{vvisc}} + \underbrace{\tilde{D}_v}_{\text{hvisc}}, \tag{B2}$$

in which the curvilinear transformation term (CT) is given by

$$\begin{aligned} CT = {} & \frac{H_Z\tilde{u}\tilde{v}}{mn}\frac{\partial}{\partial \tilde{x}}\left(\frac{mn}{H_Z}\right) + \frac{H_Z\tilde{v}\tilde{v}}{mn}\frac{\partial}{\partial \tilde{y}}\left(\frac{mn}{H_Z}\right) \\ & + m(\tilde{u}\sin\theta + \tilde{v}\cos\theta)(\tilde{u}\cos\theta - \tilde{v}\sin\theta)\frac{\partial}{\partial \tilde{x}}\left(\frac{1}{m}\right) \\ & + m(\tilde{u}\cos\theta - \tilde{v}\sin\theta)^2\frac{\partial}{\partial \tilde{y}}\left(\frac{1}{m}\right) \\ & - n(\tilde{u}\sin\theta + \tilde{v}\cos\theta)(\tilde{u}\cos\theta - \tilde{v}\sin\theta)\frac{\partial}{\partial \tilde{x}}\left(\frac{1}{n}\right) \\ & + n(\tilde{u}\sin\theta + \tilde{v}\cos\theta)^2\frac{\partial}{\partial \tilde{y}}\left(\frac{1}{n}\right). \end{aligned} \tag{B3}$$

Here $(\tilde{u}, \tilde{v})$ are the velocity components in the along- and cross-channel directions, Ω is the velocity component in the σ-direction, m and n are the scale factors that relate the differential distances in ξ-η grid to the actual (physical) arc lengths, $H_z = \partial z/\partial\sigma$, and $\tilde{D}_v$ represents the horizontal viscosity terms. All the terms in the two horizontal momentum equations are calculated in the diagnostics package provided by ROMS. They can be combined to yield the terms in the along- and cross-channel momentum equations using the decomposition method described in Appendix A.

[42] To obtain the equation for the streamwise vorticity, we take the vertical derivative of equation (B2) and make use of $\frac{\partial}{\partial z} = \frac{1}{H_Z}\frac{\partial}{\partial \sigma}$. In the transformed coordinate system, the streamwise vorticity is given by

$$\omega_x = -\frac{1}{H_Z}\frac{\partial \tilde{v}}{\partial \sigma} \tag{B4}$$

and the equation of the streamwise vorticity becomes

$$\frac{\partial \omega_x}{\partial t} = \overbrace{\frac{f}{H_Z}\frac{\partial \tilde{u}}{\partial \sigma}}^{\text{tilting of planetary vorticity}} + \overbrace{\frac{1}{H_Z}\frac{\partial}{\partial \sigma}\left(\frac{1}{\rho}\frac{\partial P}{\partial \tilde{y}} + \frac{g\rho}{\rho_0}\frac{\partial z}{\partial \tilde{y}}\right)}^{\text{baroclinicity}} + \overbrace{\frac{1}{H_Z}\frac{\partial}{\partial \sigma}\left(\frac{\partial \tilde{u}\tilde{v}}{\partial \tilde{x}} + \frac{\partial \tilde{v}\tilde{v}}{\partial \tilde{y}} - CT + \frac{1}{H_Z}\frac{\partial(H_Z\tilde{v}\Omega)}{\partial \sigma}\right)}^{\text{nonlinear advection}} \underbrace{-\frac{1}{H_Z^2}\frac{\partial^2}{\partial \sigma^2}\left(\frac{K_V}{H_Z}\frac{\partial \tilde{v}}{\partial \sigma}\right)}_{\text{vertical diffusion}} \underbrace{-\frac{1}{H_Z}\frac{\partial \tilde{D}_v}{\partial \sigma}}_{\text{horizontal diffusion}}. \tag{B5}$$

The nonlinear advection term is zero if the variation in along-channel direction is zero, as assumed in the derivation of equation (8). In all the model runs considered in this paper, the nonlinear advection term and horizontal diffusion terms are much smaller than the other terms in the streamwise vorticity equation.

[43] In this paper we integrate equation (B5) over a control volume to examine the overall balance in the streamwise vorticity equation. The volume integration is defined as

$$\overline{\omega}_x = \frac{\oiint_A \overline{\omega}_x^{depth} dA}{\oiint_A dA}, \tag{B6}$$

where $\overline{\omega}_x^{depth} = \dfrac{\int_{-h}^{\varsigma} \omega_x dz}{\int_{-h}^{\varsigma} dz}$ and A is the surface area of the selected region.

[44] **Acknowledgments.** We thank Bill Boicourt, Malcolm Scully and Peng Jia for helpful discussions. We are grateful to NSF (OCE-082543 and OCE-0961880) and NOAA (CHRP-NA07N054780191) for the financial support. This is UMCES contribution 4682 and CHRP contribution 168.

References

Burchard, H., and H. M. Schuttelaars (2012), Analysis of tidal straining as driver for estuarine circulation in well-mixed estuaries, *J. Phys. Oceanogr.*, *42*(2), 261–271, doi:10.1175/JPO-D-11-0110.1.

Burchard, H., R. D. Hetland, E. Schulz, and H. M. Schuttelaars (2011), Drivers of residual estuarine circulation in tidally energetic estuaries: Straight and irrotational channels with parabolic cross section, *J. Phys. Oceanogr.*, *41*(3), 548–570, doi:10.1175/2010JPO4453.1.

Chant, R. J. (2002), Secondary circulation in a region of flow curvature: Relationship with tidal forcing and river discharge, *J. Geophys. Res.*, *107*(C9), 3131, doi:10.1029/2001JC001082.

Chen, S.-N., and L. P. Sanford (2009), Axial wind effects on stratification and longitudinal salt transport in an idealized, partially mixed estuary, *J. Phys. Oceanogr.*, *39*(8), 1905–1920, doi:10.1175/2009JPO4016.1.

Chen, S.-N., L. P. Sanford, and D. K. Ralston (2009), Lateral circulation and sediment transport driven by axial winds in an idealized, partially mixed estuary, *J. Geophys. Res.*, *114*, C12006, doi:10.1029/2008JC005014.

Cheng, P., R. E. Wilson, R. J. Chant, D. C. Fugate, and R. D. Flood (2009), Modeling influence of stratification on lateral circulation in a stratified estuary, *J. Phys. Oceanogr.*, *39*(9), 2324–2337, doi:10.1175/2009JPO4157.1.

Csanady, G. T. (1973), Wind-induced barotropic motions in long lakes, *J. Phys. Oceanogr.*, *3*(4), 429–438, doi:10.1175/1520-0485(1973)003<0429:WIBMIL>2.0.CO;2.

Friedrichs, C. T., and J. M. Hamrick (1996), Effects of channel geometry on cross sectional variations in along channel velocity in partially stratified estuaries, in *Buoyancy Effects on Coastal and Estuarine Dynamics*, *Coastal Estuarine Stud. Ser.*, vol. 53, edited by D. G. Aubrey and C. T. Friedrichs, pp. 283–300, AGU, Washington, D. C., doi:10.1029/CE053p283.

Garvine, R. W. (1985), A simple-model of estuarine subtidal fluctuations forced by local and remote wind stress, *J. Geophys. Res.*, *90*(C6), 1945–1948, doi:10.1029/JC090iC06p11945.

Garvine, R. W. (1995), A dynamical system for classifying buoyant coastal discharges, *Cont. Shelf Res.*, *15*(13), 1585–1596, doi:10.1016/0278-4343(94)00065-U.

Geyer, W. R. (1997), Influence of wind on dynamics and flushing of shallow estuaries, *Estuarine Coastal Shelf Sci.*, *44*(6), 713–722, doi:10.1006/ecss.1996.0140.

Geyer, W. R., J. D. Woodruff, and P. Traykovski (2001), Sediment transport and trapping in the Hudson River estuary, *Estuaries Coasts*, *24*(5), 670–679, doi:10.2307/1352875.

Guo, X. Y., and A. Valle-Levinson (2008), Wind effects on the lateral structure of density-driven circulation in Chesapeake Bay, *Cont. Shelf Res.*, *28*(17), 2450–2471, doi:10.1016/j.csr.2008.06.008.

Haidvogel, D. B., H. G. Arango, K. Hedstrom, A. Beckmann, P. Malanotte-Rizzoli, and A. F. Shchepetkin (2000), Model evaluation experiments in the North Atlantic Basin: Simulations in nonlinear terrain-following coordinates, *Dyn. Atmos. Oceans*, *32*(3), 239–281, doi:10.1016/S0377-0265(00)00049-X.

Huijts, K., H. Schuttelaars, H. De Swart, and C. Friedrichs (2009), Analytical study of the transverse distribution of along-channel and transverse residual flows in tidal estuaries, *Cont. Shelf Res.*, *29*(1), 89–100, doi:10.1016/j.csr.2007.09.007.

Janzen, C. D., and K. C. Wong (2002), Wind-forced dynamics at the estuary-shelf interface of a large coastal plain estuary, *J. Geophys. Res.*, *107*(C10), 3138, doi:10.1029/2001JC000959.

Kundu, P. K., and I. M. Cohen (2004), *Fluid Mechanics*, 3rd ed., 759 pp., Elsevier Acad., San Diego, Calif.

Lacy, J. R., M. T. Stacey, J. R. Burau, and S. G. Monismith (2003), Interaction of lateral baroclinic forcing and turbulence in an estuary, *J. Geophys. Res.*, *108*(C3), 3089, doi:10.1029/2002JC001392.

Lerczak, J. A., and W. R. Geyer (2004), Modeling the lateral circulation in straight, stratified estuaries, *J. Phys. Oceanogr.*, *34*(6), 1410–1428.

Li, M., and L. J. Zhong (2009), Flood-ebb and spring-neap variations of mixing, stratification and circulation in Chesapeake Bay, *Cont. Shelf Res.*, *29*(1), 4–14, doi:10.1016/j.csr.2007.06.012.

Li, M., L. Zhong, and W. C. Boicourt (2005), Simulations of Chesapeake Bay estuary: Sensitivity to turbulence mixing parameterizations and comparison with observations, *J. Geophys. Res.*, *110*, C12004, doi:10.1029/2004JC002585.

Li, M., L. Zhong, W. C. Boicourt, S. L. Zhang, and D. L. Zhang (2007), Hurricane-induced destratification and restratification in a partially mixed estuary, *J. Mar. Res.*, *65*(2), 169–192.

Li, Y., and M. Li (2011), Effects of winds on stratification and circulation in a partially mixed estuary, *J. Geophys. Res.*, *116*, C12012, doi:10.1029/2010JC006893.

Malone, T. C., W. M. Kemp, H. W. Ducklow, W. R. Boynton, J. H. Tuttle, and R. B. Jonas (1986), Lateral variation in the production and fate of phytoplankton in a partially stratified estuary, *Mar. Ecol. Prog. Ser.*, *32*(2–3), 149–160, doi:10.3354/meps032149.

Marchesiello, P., J. McWilliams, and A. Shchepetkin (2001), Open boundary conditions for long-term integration of regional oceanic models, *Ocean Modell.*, *3*(1–2), 1–20, doi:10.1016/S1463-5003(00)00013-5.

Monismith, S. (1986), An experimental-study of the upwelling response of stratified reservoirs to surface shear-stress, *J. Fluid Mech.*, *171*, 407–439, doi:10.1017/S0022112086001507.

Nunes, R., and J. Simpson (1985), Axial convergence in a well-mixed estuary, *Estuarine Coastal Shelf Sci.*, *20*(5), 637–649, doi:10.1016/0272-7714(85)90112-X.

Reyes-Hernández, C., and A. Valle-Levinson (2010), Wind modifications to density-driven flows in semienclosed, rotating basins, *J. Phys. Oceanogr.*, *40*(7), 1473–1487, doi:10.1175/2010JPO4230.1.

Reynolds-Fleming, J. V., and R. A. Luettich (2004), Wind-driven lateral variability in a partially mixed estuary, *Estuarine Coastal Shelf Sci.*, *60*(3), 395–407, doi:10.1016/j.ecss.2004.02.003.

Sanford, L. P., K. G. Sellner, and D. L. Breitburg (1990), Covariability of dissolved-oxygen with physical processes in the summertime Chesapeake Bay, *J. Mar. Res.*, *48*(3), 567–590.

Scully, M. E. (2010), Wind modulation of dissolved oxygen in Chesapeake Bay, *Estuaries Coasts*, *33*(5), 1164–1175, doi:10.1007/s12237-010-9319-9.

Scully, M. E., W. R. Geyer, and J. A. Lerczak (2009), The influence of lateral advection on the residual estuarine circulation: A numerical modeling study of the Hudson River estuary, *J. Phys. Oceanogr.*, *39*(1), 107–124, doi:10.1175/2008jpo3952.1.

Valle-Levinson, A. (2008), Density-driven exchange flow in terms of the Kelvin and Ekman numbers, *J. Geophys. Res.*, *113*, C04001, doi:10.1029/2007JC004144.

Wang, D. P. (1979), Wind-driven circulation in the Chesapeake Bay, winter 1975, *J. Phys. Oceanogr.*, *9*(3), 564–572, doi:10.1175/1520-0485(1979)009<0564:WDCITC>2.0.CO;2.

Warner, J. C., W. R. Geyer, and J. A. Lerczak (2005), Numerical modeling of an estuary: A comprehensive skill assessment, *J. Geophys. Res.*, *110*, C05001, doi:10.1029/2004JC002691.

Weisberg, R. H., and W. Sturges (1976), Velocity observations in the West Passage of Narragansett Bay: A partially mixed estuary, *J. Phys. Oceanogr.*, *6*(3), 345–354, doi:10.1175/1520-0485(1976)006<0345:VOITWP>2.0.CO;2.

Wilson, R. E., R. L. Swanson, and H. A. Crowley (2008), Perspectives on long-term variations in hypoxic conditions in western Long Island Sound, *J. Geophys. Res.*, *113*, C12011, doi:10.1029/2007JC004693.

Winant, C. (2004), Three-dimensional wind-driven flow in an elongated, rotating basin, *J. Phys. Oceanogr.*, *34*(2), 462–476, doi:10.1175/1520-0485(2004)034<0462:TWFIAE>2.0.CO;2.

Wong, K. C. (1994), On the nature of transverse variability in a coastal-plain estuary, *J. Geophys. Res.*, *99*(C7), 14,209–14,222, doi:10.1029/94JC00861.

Zhong, L., and M. Li (2006), Tidal energy fluxes and dissipation in the Chesapeake Bay, *Cont. Shelf Res.*, *26*(6), 752–770, doi:10.1016/j.csr.2006.02.006.

Zhong, L., M. Li, and M. G. G. Foreman (2008), Resonance and sea level variability in Chesapeake Bay, *Cont. Shelf Res.*, *28*(18), 2565–2573, doi:10.1016/j.csr.2008.07.007.